

8. N. K. Humphrey, in *Growing Points in Ethology*, P. G. Bateson, R. A. Hinde, Eds. (Cambridge Univ. Press, Cambridge, 1976), pp. 303–321.
9. F. B. M. de Waal, *Chimpanzee Politics: Power and Sex Among Apes* (Harper and Row, New York, 1982).
10. R. W. Byrne, A. Whiten, Eds. *Machiavellian Intelligence: Social Expertise and the Evolution of Intellect in Monkeys, Apes and Humans* (Clarendon Press, Oxford, 1988).
11. R. I. M. Dunbar, *Annu. Rev. Anthropol.* **32**, 163 (2003).
12. R. Boyd, P. J. Richerson, *Proc. Br. Acad.* **88**, 77 (1996).
13. L. S. Vygotsky, *Mind in Society: The Development of Higher Psychological Processes* (Harvard Univ. Press, Cambridge, MA, 1978).
14. A. Whiten et al., *Nature* **399**, 682 (1999).
15. C. P. van Schaik et al., *Science* **299**, 102 (2003).
16. M. Tomasello, *The Cultural Origins of Human Cognition* (Harvard Univ. Press, Cambridge, MA, 1999).
17. R. I. M. Dunbar, *J. Hum. Evol.* **22**, 469 (1992).
18. R. I. M. Dunbar, *Behav. Brain Sci.* **16**, 681 (1993).
19. R. I. M. Dunbar, *Evol. Anthropol.* **6**, 178 (1998).
20. H. Kudo, R. I. M. Dunbar, *Anim. Behav.* **62**, 711 (2001).
21. R. O. Deaner, C. P. van Schaik, V. E. Johnson, *Evol. Psychol.* **4**, 149 (2006).
22. M. Tomasello, J. Call, *Primate Cognition* (Oxford Univ. Press, New York, 1997).
23. D. L. Cheney, R. M. Seyfarth, *How Monkeys See the World: Inside the Mind of Another Species* (Univ. of Chicago Press, Chicago, 1990).
24. D. L. Cheney, R. M. Seyfarth, *Baboon Metaphysics: The Evolution of a Social Mind* (Univ. of Chicago Press, Chicago, 2007).
25. See supporting material on Science Online.
26. A. Whiten, in *Theories of Theories of Mind*, P. Carruthers, P. K. Smith, Eds. (Cambridge Univ. Press, Cambridge, 1996), pp. 277–292.
27. M. D. Hauser, F. Tsao, P. Garcia, E. S. Spelke, *Proc. R. Soc. London Ser. B* **270**, 1441 (2003).
28. D. B. M. Haun, C. Rapold, J. Call, G. Janzen, S. C. Levinson, *Proc. Natl. Acad. Sci. U.S.A.* **103**, 17568 (2006).
29. H. Coqueugnot, J.-J. Hublin, F. Veillon, F. Houët, T. Jacob, *Nature* **431**, 299 (2004).
30. R. G. Klein, *The Human Career: Human Biological and Cultural Origins* (Univ. of Chicago Press, Chicago, ed. 2, 1999).
31. M. Tomasello, M. Carpenter, J. Call, T. Behne, H. Moll, *Behav. Brain Sci.* **28**, 675 (2005).
32. B. Hare, M. Brown, C. Williamson, M. Tomasello, *Science* **298**, 1634 (2002).
33. J. Bräuer, J. Kaminski, J. Call, M. Tomasello, *J. Comp. Psychol.* **120**, 38 (2006).
34. A. Fischer, J. Pollack, O. Thalman, B. Nickel, S. Pääbo, *Curr. Biol.* **16**, 1133 (2006).
35. D. Voyer, S. Voyer, M. Bryden, *Psychol. Bull.* **117**, 250 (1995).
36. J. C. Venter et al., *Science* **291**, 1304 (2001).
37. E. S. Lander et al., *Nature* **409**, 860 (2001).
38. The Chimpanzee Sequencing and Analysis Consortium, *Nature* **437**, 69 (2005).
39. M. Hauser, *Nature* **437**, 60 (2005).
40. We thank L. Pharoah, R. Atencia, K. Brown, and the Jane Goodall Institute USA and staff of Tchimpounga Sanctuary, as well as L. Ajarova, D. Cox, R. Ssunna, and the trustees and staff of Ngamba Island Chimpanzee Sanctuary, for their enthusiasm, help, and support. We also thank B. M. Galdikas and the staff of the Orangutan Care Center and Quarantine in Pasir Panjang for their great help and support. In particular, we appreciate the hard work of the animal caregivers from the three sanctuaries: J. Maboto, B. Moubaka, A. Sitou, M. Makaya, B. Bissafi, C. Ngoma, W. Bouity, J. A. Tchikaya, L. Bibimbou, A. Makosso, C. Boukindi, G. Nzaba, B. Ngoma, P. Kibirege, I. Mujaasi, S. Nyandwi L. Mugisha, M. Musumba, G. Muyingo, P. Mekok, P. Usai, and P. Yoyong. We also appreciate the permission from the Ugandan National Council for Science and Technology and the Uganda Wildlife Authority, as well as the Congolese Ministère de la Recherche Scientifique et de l'Innovation Technique, the Indonesian Institute of Sciences (LIPI), and the Indonesian Ministry of Forestry for allowing us to conduct our research in their countries. Special thanks go to A. Loose, M. Schäfer, K. Greve, E. Graf, V. Wobber, J. Cissewski, and S. Hastings for their enormous help with organizing, data collection and coding. In addition, we thank J. Uebel, L. Jorschik, A. Gampe, H. Roethel, K. Haberl, A. P. Melis, J. Riedel, D. Hanus, S. Girlich, P. Jahn, C. Gerisch, S. Rolle, A. Buergermeister, L. Gieselmann, D. Lagner, J. Kramareva, A. Misch, S. Helmig, E. Scholl, and A. Rosati for their various help to make this study successful. Thanks to D. Haun for helpful comments on the manuscript. We also thank the parents and children who participated in the study. The research of B.H. is supported by a Sofja Kovalevskaja award from the Alexander von Humboldt Foundation and the German Federal Ministry for Education and Research. The research of E.H. is supported by a grant from the Studienstiftung des Deutschen Volkes.

Supporting Online Material

www.sciencemag.org/cgi/content/full/317/5843/1360/DC1
 Materials and Methods
 SOM Text
 Figs. S1 and S2
 Tables S1 to S7
 References
 Movies S1 to S32
 11 June 2007; accepted 24 July 2007
 10.1126/science.1146282

REPORTS

Muscular Thin Films for Building Actuators and Powering Devices

Adam W. Feinberg,¹ Alex Feigel,² Sergey S. Shevkopyas,² Sean Sheehy,¹
 George M. Whitesides,^{2*} Kevin Kit Parker^{1*}

We demonstrate the assembly of biohybrid materials from engineered tissues and synthetic polymer thin films. The constructs were built by culturing neonatal rat ventricular cardiomyocytes on polydimethylsiloxane thin films micropatterned with extracellular matrix proteins to promote spatially ordered, two-dimensional myogenesis. The constructs, termed muscular thin films, adopted functional, three-dimensional conformations when released from a thermally sensitive polymer substrate and were designed to perform biomimetic tasks by varying tissue architecture, thin-film shape, and electrical-pacing protocol. These centimeter-scale constructs perform functions as diverse as gripping, pumping, walking, and swimming with fine spatial and temporal control and generating specific forces as high as 4 millinewtons per square millimeter.

Muscle cells are microscale linear actuators driven by the activation of actin-myosin motors, coordinated in space and time through excitation-contraction (EC) coupling (1, 2). Structure-function relations are conserved over several orders of spatial magnitude, from the sarcomere to the muscle bundle, by virtue of a hierarchical architecture. These architectures are achieved by morphogenesis programs that are responsible for coupling a

broad range of processes, from sarcomeregenesis to the integration of the biochemical and electrical networks that support muscle function (1). Muscle actuation occurs over a wide range of frequencies (0 to ~100 Hz), spatial dimensions (5 μm to ≥ 1 m), and force regimes (~5 μN to ≥ 1 kN) (3, 4). Artificial muscles can match certain temporal, spatial, or force regimes typical of biological muscle (5, 6), but they cannot fully replicate all of these capabilities, nor can they use

the same high-density energy sources. Thus, engineered muscle remains an attractive method for building actuators and powering devices from the micro to macro scales.

Device design with engineered tissues faces many of the same technical challenges as therapeutic cardiac tissue engineering [reviewed in (7)], the most difficult of which is proper replication of morphogenetic coupling schemes in three dimensions. Tissue-engineered myocardium based on cardiomyocytes seeded into gels (8), rolled up from sheets (9), or released from surfaces (10) has demonstrated the potential to produce actuators (11), tissue grafts (12), and power microdevices (13). The utility of these techniques is limited by the geometry of the device, but recent work in soft lithography (14–16) has provided new techniques to replicate cell and tissue microenvironments in vitro, suggesting an alternative means of achieving the functionality of a three-dimensional (3D) device with a 2D tissue.

¹Disease Biophysics Group, School of Engineering and Applied Sciences, Harvard University, Cambridge, MA 02138, USA.
²Department of Chemistry and Chemical Biology, Harvard University, Cambridge, MA 02138, USA.

*To whom correspondence should be addressed. E-mail: gw Whitesides@gmwhgroup.harvard.edu (G.M.W.); kkparker@seas.harvard.edu (K.K.P.)

We reasoned that to mimic the functionality of muscle bundles, a 2D engineered muscle tissue on a free-standing, flexible thin film would allow three degrees of freedom during contraction. We built 2D anisotropic cardiac tissues by culturing neonatal rat ventricular cardiomyocytes on polydimethylsiloxane (PDMS) elastomer thin films, muscular thin films (MTFs), which remained planar during myogenesis and then were shaped and released into 3D. Shortening of cardiomyocytes during synchronous contraction caused the PDMS thin film to bend during systole (contraction) and return to its original shape during diastole (relaxation). Based on the ability of these 2D planar shapes to adopt complex 3D conformations (17, 18), we leveraged the inherent contractility of the cardiomyocytes to create a variety of proof-of-concept 3D actuators and soft robotic devices.

We engineered three kinds of 2D myocardial tissue: isotropic (Fig. 1, A to C), anisotropic 2D (Fig. 1, D to F), or an array of discrete muscle fibers (Fig. 1, G to I) by passive seeding of dissociated ventricular cardiomyocytes on fibronectin (FN)-coated or microcontact-printed (μ CP) surfaces (14, 15). Each tissue type was characterized by distinct differences in sarcomere alignment (i.e., direction of contractility) as well as

electromechanical coupling (fig. S1) (19). Isotropic 2D myocardium had no net alignment of cell bodies (Fig. 1A) or sarcomeres (Fig. 1C). Anisotropic 2D myocardium had uniaxial alignment of cell bodies (Fig. 1D) and sarcomeres (Fig. 1F), fabricated by μ CP of alternating high- and low-density FN lines based on previously described methods (16). The array of discrete muscle fibers was similarly fabricated by using μ CP of FN lines and had uniaxial alignment of cell bodies (Fig. 1G) and sarcomeres (Fig. 1I). However, the electrical isolation between the fibers prevented spontaneous contraction of a single fiber from causing the entire MTF to contract (fig. S1). For both kinds of anisotropic tissue, the FN lines served as geometric cues for the inter- and intracellular organization of cardiomyocytes into a tissue and the uniaxial coupling of sarcomere ensembles over length scales from microns to centimeters.

Polymeric thin films were built by spin coating a thermally sensitive sacrificial layer of poly (N-Isopropylacrylamide) (PIPAAm) on glass cover slips and then spin coating a PDMS thin film on top of the PIPAAm (fig. S2) (19). The thickness of the PDMS film (14 to 60 μ m) was controlled by varying the viscosity of the PDMS prepolymer and the spin-coating speed (fig. S3).

Once cured, cardiomyocytes were seeded onto the FN functionalized PDMS/PIPAAm-coated cover slips and cultured at 37°C for 4 to 6 days until a 2D myocardium was formed. At 37°C, PIPAAm was hydrophobic and remained solid when in contact with water, which ensured that the PDMS remained on the cover slip. When removed from the incubator and cooled to room temperature (\sim 22°C), the desired MTF shape was manually prepared with a scalpel; aqueous dissolution of the thermally sensitive PIPAAm layer released the MTF. The PDMS thus served as a detachable, biocompatible substrate for the 2D tissue. Once in solution, the MTF spontaneously adopted a 3D conformation determined by its film properties or was fashioned to create more complex 3D shapes. While the cardiomyocytes provided either spontaneous or paced contractile function, the PDMS thin film allowed mesoscale sculpting of functional forms, restorative elasticity, and improved handling characteristics. Specifically, the PDMS film thickness dictated MTF bending stiffness, and its structural integrity allowed the muscle sheet to be formed into a variety of 3D shapes without disrupting the 2D muscle tissue.

The 3D deflection of MTFs depended on the direction of tissue alignment relative to the PDMS thin-film geometry (fig. S4 and movie S1). For example, on similarly sized rectangles, aligning anisotropic 2D myocardium along the width (fig. S4A), length (fig. S4B), and diagonal (fig. S4C) resulted in deformation along those axes with minimal deformation along the orthogonal axes. These results illustrate the relation between uniaxial sarcomere alignment (Fig. 1F) and contraction (fig. S4). A similar correlation has been reported between cardiomyocyte alignment and longitudinal and transverse conduction velocities in anisotropic 2D myocardium (16).

To test our hypothesis that the constructs would display biomimetic functionality, we fabricated simple oscillators, soft robotic actuators, and motile devices that could walk and swim. Soft robotic actuators were constructed with MTFs by controlling process parameters and EC coupling to dictate the 3D conformation of the free-standing construct and the contraction kinetics (19). Thin-film thickness (fig. S3) could be varied to control diastolic MTF conformation. The elastic modulus for Sylgard 184 PDMS elastomer is 1.5 MPa (20), whereas the elastic modulus for rat cardiomyocytes is \sim 30 kPa (21), a difference of two orders of magnitude. The MTF bending stiffness was dominated by the PDMS, which ranged from 0.5 to 30 μ N/m. MTFs, for which the PDMS thickness was greater than \sim 25 μ m, remained planar during diastole. In contrast, thinner films adopted a curved conformation as soon as the MTFs were released from the cover slips (Fig. 2), which defined two possible modes of systolic film bending, flexion, or extension. Which surface cardiomyocytes were on, convex or concave, was controlled by the cure temperature of the

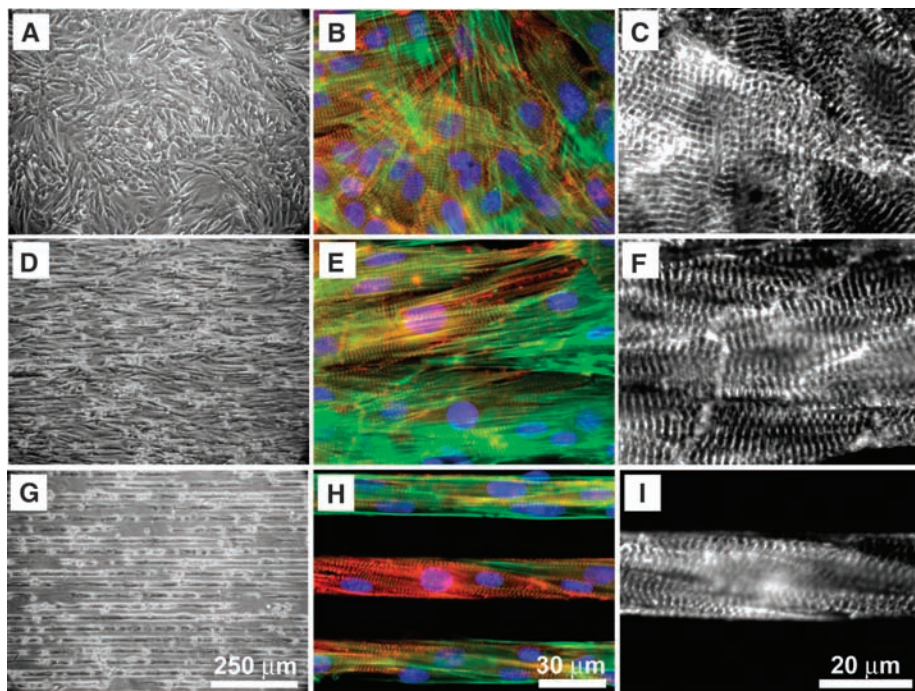


Fig. 1. The microstructure of the 2D myocardium was engineered to be isotropic or anisotropic to control contractility. Uniform FN coatings produced isotropic 2D myocardium (A to C) with no long-range order. (C) Staining for sarcomeric α -actinin revealed no preferential alignment of sarcomeres along any axis. Micropatterns of alternating high- and low-density 20- μ m-wide FN lines (D to F) produced continuous anisotropic 2D myocardium. (F) Staining for sarcomeric α -actinin revealed uniaxial sarcomere alignment. Micropatterns of alternating 20- μ m-wide lines of high density FN and Pluronic F127 (BASF Corp., Florham Park, New Jersey, USA) (G to I) produced an array of discrete muscle fibers. (I) Staining for sarcomeric α -actinin revealed uniaxial sarcomere alignment. Images are phase contrast [(A), (D), and (G)]; immunofluorescence of nuclei (blue), F-actin (green) and sarcomeric α -actinin (red) [(B), (E), and (H)]; and the signal from sarcomeric α -actinin alone [(C), (F), and (I)] to indicate and emphasize the direction of sarcomere alignment.

PDMS, 22°C (room-temperature cure) or 65°C (heat cure), respectively (19). We designed a number of 2D shapes as templates engineered to adopt defined 3D conformations after release from the cover slip.

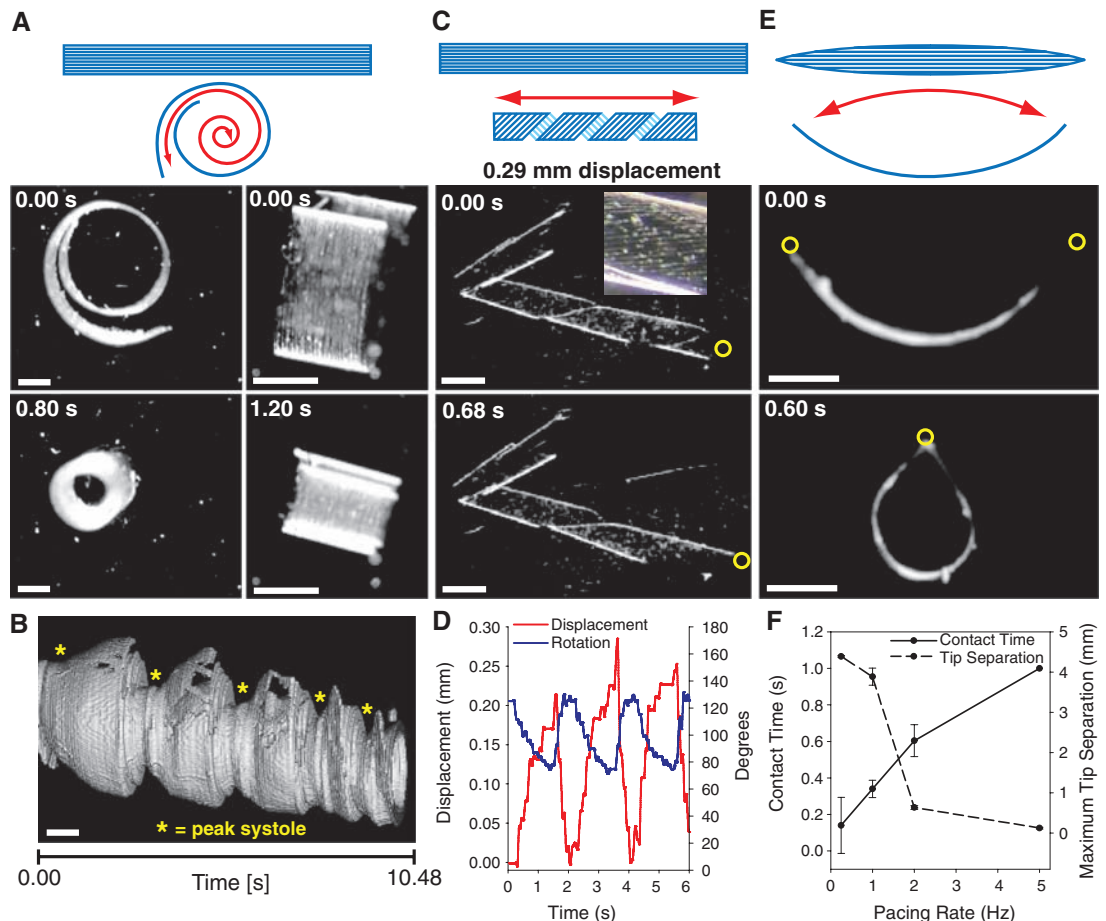
When MTFs with 2D myocardium on the concave surface contracted, the radius of film curvature decreased, bending the film further out of plane (flexion). For example, long rectangular strips with anisotropic 2D tissue aligned along their length (Fig. 2A). In this configuration, the MTF transitioned from a loosely rolled state (diastole) to a tightly rolled state (systole) during spontaneous, cyclic contractions (movie S2). The stress produced by this rolled MTF at peak systole was at least 15 kPa per contraction [calculated by measuring MTF radius of curvature at peak systole and solving a modified Stoney's equation (fig. S5) (19)]. MTF contraction was faster than relaxation; this temporal asymmetry was measured by plotting change in the diameter as a function of time (Fig. 2B and movie S2). This feature has application in valveless pumping of viscous fluids similar to the embryonic vertebrate heart tube by peristaltic action (22) or hydroelastic impedance (23). Further, these rolled MTFs are reminiscent of

the laminar structure of the ventricle, where anisotropic sheets of cardiac muscle are wrapped to form a cavity whose blood-filled volume is reduced during systole (24).

When MTFs engineered with 2D myocardium on the convex surface contracted, the radius of film curvature increased (or even inverted), bending the film back in plane (extension). We made helical MTF actuators capable of cyclic, axial extension and rotation created by aligning an array of discrete muscle fibers 5° to 15° off-axis to the length of long PDMS rectangles (Fig. 2C). These constructs spontaneously adopted this helical conformation (like a paper towel tube), where the pitch was a function of the angle between the longitudinal axis of the anisotropic tissue and the midline of the thin film. Contraction of the MTF resulted in a decrease in helical pitch while maintaining a constant inner radius (movie S3), producing ~300 μm of axial extension and ~50° of circumferential rotation (Fig. 2D). Although this is in contrast to the rolling laminar structure depicted in Fig. 2A, this functional scheme is consistent with alternative theories of diastolic ventricular function which suggest that the ventricles can act as a suction pump (25).

We built a soft robotic gripper that uses electrical stimulation protocols to produce tonic contraction of the MTF with prescribed strength and grip radius (Fig. 2E and movie S4). An electric field was created using parallel, platinum wire electrodes on either side of the gripper, and a function generator controlled voltage amplitude (10 V, 10 ms pulse-width) and stimulation frequency (19). Specifically, pacing frequency was modulated from 0.25 to 5.0 Hz to control systolic bending of the gripper and hold the longitudinal ends at a prescribed separation (Fig. 2F). During contraction, the ends of the gripper come together until they touch and stop due to the contact force. Rather than simply opening and closing once, the gripper was switched from an open state (diastole) to a tonic, closed state during systole by increasing the pacing rate until the MTF entered tetanus at 5 Hz [generating constant stress in excess of 25 kPa (fig. S6)]. So, whereas gripping objects by hand is achieved by increased firing rate and motor unit recruitment, in our devices, we could accomplish this only with the former (26). Shaping and functionalizing of the distal ends of the gripper has potential for enabling tasks such as binding and manipulation of single cells and small biological samples.

Fig. 2. MTFs were used to build soft robotic actuators with customized functionality. (A) The coiled strip had anisotropic myocardium (on the concave surface) aligned along the rectangle length that cyclically contracts from an uncoiled to coiled state. (B) This is a 3D plot of the coiled strip's diameter as a function of time, where peak systole is noted with asterisks. This shows the temporal asymmetry between the rapid coiling rate (contraction) compared with the slower uncoiling rate (relaxation). (C) The helical linear actuator was a rectangular strip with discrete arrayed muscle fibers [on the convex surface (see inset)] that spontaneously adopted a helical conformation. (D) Tracking the tips [yellow circles in (C)] shows cyclic extension and rotation at 0.5 Hz pacing. (E) The "gripper" was a long, rectangular strip with lengthwise-aligned anisotropic myocardium (on the concave surface) that brought the tips together upon contraction. (F) Tracking the tips [yellow circles in (E)] as a function of pacing rate demonstrated control of diastolic tip separation and the period the gripper was closed per second (error bars represent SD). For each MTF, the schematic illustrates the 2D shape and cardiomyocyte alignment before release and the subsequent 3D conformation [red arrows in (A), (C),



and (E) indicate direction of film bending]. The video still images show the construct in diastole at time 0.00 s and in systole 0.60 to 1.20 s later. Scale bars, 1 mm.

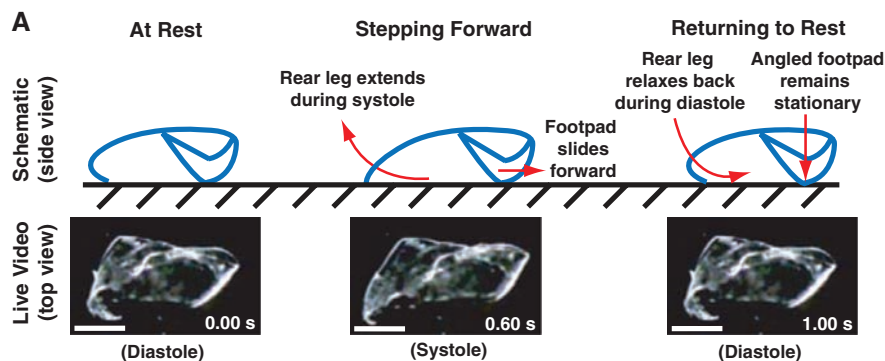
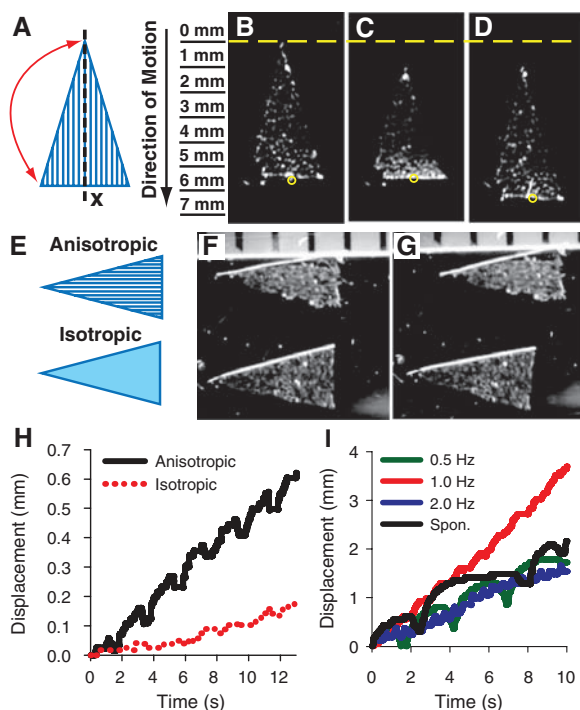


Fig. 3. Myopod capable of autonomous or remote-controlled walking. The myopod was formed from a triangle MTF, with isotropic myocardium (on the convex surface) manually folded into a 3D shape. (A) The motion is illustrated in a schematic side view and live top view as it starts in diastole and steps forward during systole. During systole the myocardium contracted, causing the “leg” to extend and push the myopod forward. As the leg relaxed during diastole, the angled footpad prevented the myopod from slipping backward.

(B) Frame-by-frame video tracking of the front of the myopod at 1-s intervals (denoted by black dots; linear regression denoted by solid line) shows consistent and directed locomotion at a speed of ~8 mm/min at 1 Hz pacing (10 V amplitude). Myopod relative velocity (~2.7 lengths/min) is similar to that reported by Xi *et al.* (~3.7 lengths/min) for their muscle-powered microdevice (13); however, the myopod can be reconfigured by refolding it into another conformation and does not require microfabrication to build. Scale bars, 1 mm.

Fig. 4. The triangular MTF swimmers demonstrate that tissue microstructure, film shape, and pacing rate collectively contributed to motility. (A) The MTF triangle swimmer was realized by aligning anisotropic myocardium parallel to the height of the triangle (red arrows denote direction of film bending). Tracking the MTF through subsequent video frames showed that (B) the relaxed construct contracts by (C) pulling the tail (tip) of the triangle in toward the base. (D) As the triangle relaxed and returned to its original shape, it produced a propulsive force that drove the MTF forward. (E) Comparison of similarly shaped triangle swimmers with anisotropic or isotropic myocardium revealed the importance of tissue structure in potentiating motility. At 0.5 Hz pacing, the anisotropic swimmer, (F) starting from rest, (G) surged ahead after 13 s. (H) Tracking frame-by-frame displacement showed that the anisotropic swimmer was ~5 times as fast as the isotropic swimmer. (I) The anisotropic swimmer’s velocity was a function of pacing rate, revealing a maximum swimming rate of ~24 mm/min at 1.0 Hz pacing. Pacing voltage was 10 V except for spontaneous contractions in (I). Ruler markings in (F) and (G) are 1 mm.



loop reattached midway along the height to create a footpad (Fig. 3A). The MTFs reconfigure because the exposed PDMS is hydrophobic on the non-cell side, which sticks to itself in aqueous solution and provides a convenient way to fabricate complex 3D shapes. When paced, the myopod moved with constant velocity (Fig. 3B).

We reasoned that 2D MTFs could replicate the anguilliform swimming motion of a *Basilosaurus* with properly engineered tissue registered to the appropriate thin-film geometry. Autonomous and remotely controlled swimming MTFs were engineered from ~30- μ m-thick PDMS films cut into isosceles triangles with the anisotropic myocardium assembled parallel to the height of the thin film (Fig. 4A). Field stimulation induced a propagating contractile wave (Fig. 4, B to D) that resulted in increasingly greater orthogonal deflection of the MTF toward the tip. Comparing similar triangle swimmers with isotropic or anisotropic 2D myocardium (Fig. 4E and movie S6) demonstrated that tissue microarchitecture was critical in potentiating motility. During a typical experiment (Fig. 4, F and G), the anisotropic swimmer traveled ~5 times as far, with an average velocity of 3 mm/min. The isotropic tissue failed to contract in a manner necessary for generating propulsion, twitching and drifting at a rate of 0.6 mm/min (Fig. 4H).

As in the case of the soft robotic gripper, the electrical pacing protocol applied to the MTF swimmer could be tailored to maximize swimming velocity and minimize the metabolic cost (i.e., maximize distance traveled per contractile cycle) (Fig. 4I and movie S7). The swimming motion was separated into two phases, burst (systole) and coast (diastole, passive propulsion). This swimming technique is used by species such as the zebrafish, where a single tail flip is followed by a phase where the fish keeps its body straight (27). Maximum velocity (24 mm/min)

We can engineer MTF actuators with many functional shapes, but do they generate enough force to be useful? Isometric contraction of MTFs demonstrated specific forces of 1 to 4 mN/mm² (fig. S7), comparable to tissue engineered myocardium (8, 9) and native cardiac muscle (19). Unlike artificial muscles, MTFs demonstrate moderate contractile forces, high strain, fast actuation, and low power consumption (5, 19). On the basis of these findings, we reasoned that MTFs could move by mimicking the locomotion of simple organisms. MTFs were engineered for use as autonomous, or remotely controlled, soft robotic

vehicles. In this context, remote control refers to control of contraction rate using electrical field stimulation. Locomoting constructs, myopods, were designed to walk along the bottom of a Petri dish in a directed path under spontaneous or paced contractions (Fig. 3 and movie S5). The myopod was formed from a triangular MTF with isotropic 2D myocardium (Fig. 1A) rather than the anisotropic 2D myocardium (Fig. 1D), demonstrating that, in this case, microscale control of tissue microstructure was not required for motility. Rather, the spatial symmetry break was achieved by folding the tip of the triangle into a

was achieved at 1 Hz pacing frequency by taking advantage of this velocity profile (Fig. 4I). Slower pacing at 0.5 Hz resulted in periodic dips in the velocity as the coasting speed deteriorated before the next contractile cycle. Faster pacing at 2 Hz interrupted the power stroke before it was completed. These findings show that the stimulation frequency may be varied to optimize MTF function. Zebrafish larvae transition from low to high Reynolds number swimming by increasing tail-beat frequency and bend amplitude (degrees) and shifting bend location, which suggests that similar performance is possible with MTF swimmers (28). We have scaled this swimming behavior from $Re \sim 0.1$ to ~ 10 for 2 mm to 1.2 cm length-scale MTF swimmers. It should be possible to scale-up these swimmers further (to $Re > 100$), because zebrafish use the same burst-and-coast behavior from larvae (~ 4 mm) to adult (~ 35 mm) length-scales (27).

Can we leverage these capabilities to build more advanced soft robotic actuators and devices? One possibility is to borrow biological design principles from organisms such as octopi that use elastic, muscular appendages for complex movements such as bipedal locomotion and articulated joints (29). Another is to scale-up force generation by increasing the thickness of the 2D myocardium or by combining multiple MTFs in parallel. Beyond devices, analysis of MTF deformation during contraction also has

potential for studying biomechanics of myocardial sheets as a model for the laminar muscle of the ventricular wall.

References and Notes

1. D. M. Bers, *Excitation-Contraction Coupling and Cardiac Contractile Force* (Kluwer, Boston, ed. 2, 2001).
2. D. M. Bers, *Nature* **415**, 198 (2002).
3. A. J. Brady, S. T. Tan, N. V. Ricciuti, *Nature* **282**, 728 (1979).
4. S. Nishimura *et al.*, *Am. J. Physiol. Heart Circ. Physiol.* **287**, H196 (2004).
5. J. D. W. Madden *et al.*, *IEEE J. Ocean. Eng.* **29**, 706 (2004).
6. V. H. Ebron *et al.*, *Science* **311**, 1580 (2006).
7. W. H. Zimmermann *et al.*, *Cardiovasc. Res.* **71**, 419 (2006).
8. W. H. Zimmermann, I. Melnychenko, T. Eschenhagen, *Biomaterials* **25**, 1639 (2004).
9. K. Baar *et al.*, *FASEB J.* **19**, 275 (2005).
10. T. Shimizu, M. Yamoto, A. Kikuchi, T. Okano, *Tissue Eng.* **7**, 141 (2001).
11. Y. Tanaka, K. Sato, T. Shimizu, M. Yamato, T. Okano *et al.*, *Lab Chip* **7**, 207 (2007).
12. W. H. Zimmermann *et al.*, *Nat. Med.* **12**, 452 (2006).
13. J. Z. Xi, J. J. Schmidt, C. D. Montemagno, *Nat. Mater.* **4**, 180 (2005).
14. J. L. Tan, W. Liu, C. M. Nelson, S. Raghavan, C. S. Chen, *Tissue Eng.* **10**, 865 (2004).
15. G. M. Whitesides, E. Ostuni, S. Takayama, X. Y. Jiang, D. E. Ingber, *Annu. Rev. Biomed. Eng.* **3**, 335 (2001).
16. N. Bursac, K. K. Parker, S. Iravanian, L. Tung, *Circ. Res.* **91**, E45 (2002).
17. M. Boncheva *et al.*, *Proc. Natl. Acad. Sci. U.S.A.* **102**, 3924 (2005).

18. Y. Klein, E. Efrati, E. Sharon, *Science* **315**, 1116 (2007).
19. Materials and methods are available as supporting material on Science Online.
20. A. Olah, H. Hillborg, G. J. Vancso, *Appl. Surf. Sci.* **239**, 410 (2005).
21. S. C. Lieber *et al.*, *Am. J. Physiol. Heart Circ. Physiol.* **287**, H645 (2004).
22. M. C. Fishman, K. R. Chien, *Development* **124**, 2099 (1997).
23. A. S. Forouhar *et al.*, *Science* **312**, 751 (2006).
24. K. D. Costa, Y. Takayama, A. D. McCulloch, J. W. Covell, *Am. J. Physiol. Heart Circ. Physiol.* **276**, H595 (1999).
25. F. Torrent-Guasp *et al.*, *Eur. J. Cardiothorac. Surg.* **25**, 376 (2004).
26. S. A. Wings, M. Santello, *Integr. Comp. Biol.* **45**, 679 (2005).
27. U. K. Muller, E. J. Stamhuis, J. J. Videler, *J. Exp. Biol.* **203**, 193 (2000).
28. S. A. Budick, D. M. O'Malley, *J. Exp. Biol.* **203**, 2565 (2000).
29. C. L. Huffard, F. Boneka, R. J. Full, *Science* **307**, 1927 (2005).
30. We acknowledge financial support from the Defense Advance Research Projects Agency's Biomolecular Motors Program, the Air Force Office of Sponsored Research, and the Harvard Materials Research Science and Engineering Center (MRSEC). S.S.S. and A.F. acknowledge salary support from the U.S. Army Research Office. We thank H. Stone for comments on the manuscript.

Supporting Online Material

www.sciencemag.org/cgi/content/full/317/5843/1366/DC1

Materials and Methods

SOM Text

Figs. S1 to S7

Movies S1 to S7

22 June 2007; accepted 6 August 2007

10.1126/science.1146885

Imaging of Arsenic Cottrell Atmospheres Around Silicon Defects by Three-Dimensional Atom Probe Tomography

Keith Thompson,^{1*} Philip L. Flaitz,² Paul Ronsheim,² David J. Larson,¹ Thomas F. Kelly¹

Discrete control of individual dopant or impurity atoms is critical to the electrical characteristics and fabrication of silicon nanodevices. The unavoidable introduction of defects into silicon during the implantation process may prevent the uniform distribution of dopant atoms. Cottrell atmospheres are one such nonuniformity and occur when interstitial atoms interact with dislocations, pinning the dislocation and trapping the interstitial. Atom probe tomography has been used to quantify the location and elemental identity of the atoms proximate to defects in silicon. We found that Cottrell atmospheres of arsenic atoms form around defects after ion implantation and annealing. Furthermore, these atmospheres persist in surrounding dislocation loops even after considerable thermal treatment. If not properly accommodated, these atmospheres create dopant fluctuations that ultimately limit the scalability of silicon devices.

The controlled placement of dopant atoms and the subsequent creation of point defects in Si form the basic materials used to fabricate semiconductor field-effect devices. Each electrically "active" dopant atom contrib-

utes an electrical carrier to the lattice. A non-homogeneous distribution of dopant atoms, as measured over the nanoscale regime, could create a corresponding fluctuation in the electrical characteristics of that region. In macro-sized devices, these localized fluctuations average out over the relatively large area of the device and therefore have a negligible impact on overall performance. Now that device scales are reaching the nanometer regime, localized fluctuations are having an increasingly important impact on

the electrical characteristics of individual devices. Imaging of individual dopant atoms is essential to the development of advanced nanoscale devices and is therefore an area of intense interest among the semiconductor community (1–4).

Si wafers are most often doped with As, P, or B atoms. Because of the relatively large size of the As atom, its diffusivity is orders of magnitude lower than that of P or B. This low diffusivity makes As a desirable candidate for nanometer-scale device technology (5, 6). The ion implantation of dopant atoms, particularly the heavier As ions, almost always results in the simultaneous creation of undesired defects. The subsequent evolution of these defects as a function of thermal annealing is well documented (7–9). After ion implantation, the Si lattice is heavily damaged or possibly amorphized because the Si atoms have been ballistically removed from their lattice sites. The result is a high concentration of interstitial Si atoms, Si_i , with a corresponding supersaturation of Si vacancies, V_{Si} . The application of a small amount of thermal energy ($\sim 400^\circ$ to 600°C) is sufficient to repair the Si crystal structure. In reasonably pure Si, the Si_i atoms coalesce into energetically favorable $\{311\}$ rod-like defects (8, 9). Where a high areal concentration ($> \sim 10^{14}/\text{cm}^2$) of impurity atoms is present, the Si_i atoms instead form into spheroidal defects of varying size (8, 10). During continued thermal treatment, the spheroidal defects coalesce and grow into larger de-

¹Imago Scientific Instruments Corporation, 5500 Nobel Drive, Madison, WI 53711, USA. ²IBM Corporation, Hopewell Junction, NY 12533, USA.

*To whom correspondence should be addressed. E-mail: kthompson@imago.com